MTLA 36 (2024) 102138

Contents lists available at ScienceDirect

Materialia

journal homepage: www.elsevier.com/locate/mtla

Full length article

Finite element modeling of the magnetic property behaviors of electrical steels in rotating fields considering their crystallographic textures

Shuaichao Yue [a], Jun Liu [b,*], Yongjian Li [a,*], Guodong Liu [c]

[a] State Key Laboratory of Reliability and Intelligence of Electrical Equipment, Hebei University of Technology, Tianjin, 300130, China
[b] School of Engineering, Cardiff University, Queens Building, 14-17 The Parade, Cardiff, CF24 3AA, United Kingdom
[c] School of Materials Science and Engineering, Hebei University of Technology, Tianjin, 300130, China

ARTICLE INFO

Keywords:
Crystallographic texture
Finite element analysis
Microstructure
Magnetic anisotropy
Rotational field

ABSTRACT

In magnetic device modeling, the crystallographic textures and microstructures of electrical steels critically influence their magnetic properties. Yet, these aspects are often neglected or inadequately represented in finite element (FE) models, leading to inaccuracies in predicting electrical steel performance, especially in complex electromagnetic environments. This paper presents a multi-scale modeling approach, integrating a macroscopic FE model of a magnetic device with a microstructural scalar permeability model that accounts for the crystallographic textures of electrical steels. This approach demonstrates proficiency in predicting nonlinear anisotropic permeability and capturing magnetic anisotropy of electrical steels within a rotational tester, especially when anisotropy is predominantly governed by crystallographic texture and the angles between the **B** and **H** vectors are minimal. Furthermore, the model effectively captures the magnetic anisotropy in complex magnetic fields and geometric configurations of a permanent magnet motor. A comparative analysis of this model is conducted against three other material models: an isotropic model, a two-axis model, and a general-vector model. These models are based on different approaches, ranging from a single non-linear BH curve to comprehensive vector BH curves covering all directions. Among them, the general-vector model, reliant on extensive 2D vector BH measurements, is the most accurate but requires substantial experimental data.

1. Introduction

Electrical steels, being the predominant soft magnetic materials, constitute over 95% of production volume in this domain. They are widely used as magnetic core materials of electromagnetic devices [1, 2]. Complex rotating magnetic fields are significant in the cores of electromagnetic devices, especially at the T-joints of multiphase transformers and at the junctions between the teeth and yokes of electrical machine stators [3,4]. This complexity necessitates a comprehensive characterization of the magnetic properties of electrical steels under such fields to enhance the precision of electromagnetic numerical analyses.

The magnetic properties of electrical steels are primarily governed by the dynamics of their magnetic domains, which are significantly influenced by the material's crystallographic texture and microstructural features. Given this intricate relationship, it becomes imperative to incorporate these factors into the development of magnetic property models. Presently, most models in this field rely predominantly on mathematical curve fitting grounded in macroscopic experimental data [5–8]. Commonly used in commercial electromagnetic analysis software such as ANSYS and COMSOL, the isotropic material model typically employs a single H–B curve. This curve is either derived from measurements along the rolling direction or averaged from multiple orientations. Two-axis material models, as reported in e.g., [9,10], incorporates two B–H curves measured along orthogonal axes. This approach enables the model to capture variations in magnetic properties between these directions. On the other hand, the vector material model, detailed in [11,12], uses interpolation matrices to represent the complex interactions between ***B*** and ***H*** amplitudes and phases across various orientations, effectively accounting for material anisotropy. Although these measurement-based methods mathematically robust, they often fall short in accurately reflecting the actual magnetic behavior and the underlying physics, primarily due to the neglect of essential microstructural characteristics. This oversight can lead to considerable errors in magnetic field estimations and loss predictions within finite element (FE) modeling of electromagnetic devices. Additionally, approaches like the vector material model, necessitate the collection of substantial experimental data, further complicating the modeling process.

---

[*] Corresponding authors.
E-mail addresses: liuj118@cardiff.ac.uk (J. Liu), liyongjian@hebut.edu.cn (Y. Li).

https://doi.org/10.1016/j.mtla.2024.102138
Received 16 December 2023; Accepted 27 May 2024
Available online 30 May 2024
2589-1529/© 2024 The Author(s). Published by Elsevier B.V. on behalf of Acta Materialia Inc. This is an open access article under the CC BY license (http://creativecommons.org/licenses/by/4.0/).

FE Model Parameters

Parts	Elements	Relative Permeability
Sample	704	From the material models
Yoke	1390	5000
Coils	128	1
Air	1180	1

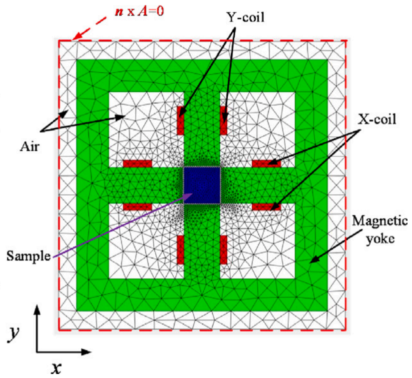

Fig. 1. Finite Element model representation of a 2D rotational tester. The inset table provides key details about the geometry and meshing and essential parameters of the model.

In addressing the prevalent challenges in the field, this paper introduces a pioneering approach by integrating a microstructural magnetic model within macroscopic FE models. This innovative model considers both the microstructure and crystallographic textures of electrical steels and can predict anisotropic permeability accurately without relying on extensive experimental measurements. This advancement significantly bolsters the efficiency and accuracy of simulating electrical steel property behaviors in rotating fields. Furthermore, our approach sheds light on the underlying mechanisms and the profound impact of magnetic anisotropy in electrical steels associated with crystallographic texture, particularly in scenarios involving complex magnetic fields and geometrical configurations. The novel integration of microstructural insights into macroscopic modeling paves the way for deeper understanding in the domain of electrical steel performance.

2. Description of the models

The present multi-scale model consists of a microstructural permeability model and a macroscopic FE magnetic device model. The former predicts anisotropic permeability given the crystallographic texture and a polycrystalline microstructure of the material. The latter takes the predicted anisotropic permeability as input defining the electrical steels in the device FE model to predict the magnetic performance of the electrical steels.

2.1. Finite element device model

Fig. 1 shows the macroscopic FE model of a simplified 2D rotational tester. It consists of a magnetic yoke with four poles, two for each axis. A square electrical steel sample is centrally located with a 2 mm air gap with the poles. The excitation coils are wound around the teeth with 80 turns each in accordance with the actual measurement system [13]. The model contains 3402 triangular elements. The number of elements and assigned material model of each part are given in the inset table in Fig. 1. First order nodal shape function is used in the FE discretization. The X-coil and Y-coil are supplied with sinusoidal currents with a 90° phase lag to force a rotational field for the sample. The 2D field problem formulated with magnetic vector potential A and fixed-point method is shown as follows

$$\nabla \times \upsilon_{FP}(\nabla \times \mathbf{A}) + \sigma \frac{\partial \mathbf{A}}{\partial t} = \mathbf{J} - \nabla \times \mathbf{M} \tag{1}$$

where υ_{FP} is the fixed-point coefficient, $\mathbf{J}$ the applied current and $\mathbf{M}$ the fixed-point residual magnetization. We choose fixed-point method for its robust convergence. It is well known that the Newton method sometimes encounters convergence problems since asymmetric or ill-conditioned Jacobian matrix may arise during iterations when dealing with materials with strong anisotropy or hysteresis. $\mathbf{M}$ is determined from the microstructural permeability model described in Section 2.2 or the measurements-based material models described in Section 2.3. More details about the FE implementation can be found elsewhere [14].

2.2. Microstructural scalar-permeability model

In our study, we use a **FE m**icrostructural magnetic model which incorporates crystallographic **tex**ture, referred to as **FEMTEX**, to predict anisotropic scalar effective permeability values. This model, elaborated in [15], utilizes microstructure data derived from electron backscatter diffraction (EBSD) to accurately define the geometry of each grain within the FE framework. In this model, every grain is considered an individual entity, characterized by its unique FE material property—specifically, its relative magnetic permeability. A uniform background magnetic flux density, B_b, is applied across the model. An External Vector Potential boundary condition is applied along the circumference of a circle, with a diameter quintuple the size of the microstructure. This configuration, implemented in COMSOL Multiphysics, simulates the air surrounding the modeled structure.

The relative permeability for a given grain i, denoted as μ_i, is derived from an empirical formula inspired by magnetocrystalline anisotropy energy, as reported in [16]:

$$\mu_i = \mu_{100} + 4(\mu_{110} - \mu_{100})(\gamma_{xi}^2\gamma_{yi}^2 + \gamma_{yi}^2\gamma_{zi}^2 + \gamma_{zi}^2\gamma_{xi}^2) + 9(3\mu_{111} + \mu_{100} - 4\mu_{110})(\gamma_{xi}^2\gamma_{yi}^2\gamma_{zi}^2) \tag{2}$$

where μ_{100}, μ_{110} and μ_{111} represent the permeability of a single crystal along the $\langle 100\rangle$, $\langle 110\rangle$ and $\langle 111\rangle$ directions respectively. The direction cosines γ_{xi}, γ_{yi} and γ_{zi} of $\mathbf{B}_b$ vector are calculated with respect to the [100], [010] and [001] respectively, using grain orientation data from EBSD. The effective permeability $\mu_e \overset{\text{def}}{=} \frac{B}{\mu_0 H}$ is averaged over the entire microstructure where μ_0 is the permeability for free space and B and H are the magnitude of the solved $\mathbf{B}$ and $\mathbf{H}$ vectors respectively.

2.3. Measurement-based material models

This section outlines three measurement-based material models, each exemplifying a distinct approach to modeling BH behavior in electrical steels. These models include an isotropic nonlinear BH behavior model and two models that approximate observed anisotropic nonlinear BH behaviors. They serve as benchmarks against the FEMTEX model.

Isotropic material model. The isotropic material model simplifies the BH relationship to a single scalar non-linear curve, denoted as $H = f(B)$, where B is along the RD. In this model, anisotropy is not considered, making it a straightforward, albeit inaccurate, representation of magnetic properties.

Two-axis material model. As a preliminary step towards capturing magnetic anisotropy, a two-axis material model is introduced. This model is based on BH curves measured along two orthogonal directions: RD and TD. Typically, the highest and lowest permeabilities are observed along the RD and TD, respectively. These curves are expressed as $H_x = f_x(B_x)$ and $H_y = f_y(B_y,)$. Scalar BH curves measured from RD and TD were used for the x and the y component respectively. This approximation is equivalent to a diagonal 2D permeability tensor, $\begin{bmatrix} \mu_{xx} & \\ & \mu_{yy} \end{bmatrix}$ where μ_{xx} and μ_{yy} are defined by $H_x = f_x(B_x)$ and $H_y = f_y(B_y)$, respectively. This approach is referred to as two-axis model in this paper.

General vector material model. For a more comprehensive representation of anisotropy, the general vector material model is introduced. In this model, the vector **H** considered as a function of the vector **B** is expressed by $H_m = f(B_m, \theta_B)$ and $\theta_H = g(B_m, \theta_B)$, where the subscript m denotes magnitude and θ_H and θ_B the direction of **H** and **B** vector with respect to RD. Functions f and g are derived from the vector BH measurements using the 2D rotational tester describe in Section 3.2. This method is equivalent to using a generalized non-diagonal non-linear permeability tensor $\begin{bmatrix} \mu_{xx} & \mu_{xy} \\ \mu_{yx} & \mu_{yy} \end{bmatrix}$.

It is important to note that none of these models – the isotropic, two-axis, or general-vector – directly incorporate crystallographic textures. Instead, they approximate the observed magnetic anisotropy based solely on experimental measurements. Whilst the FEMTEX model does require foundational microstructural data, its requirement for magnetic measurement data is significantly less extensive than that of the general-vector model, making it a more efficient option in settings where detailed microstructural data is available but extensive magnetic characterization is challenging.

3. Materials and experimental details

A commercial Grain-Oriented (GO) steel sheet of 0.27 mm thick and a non-oriented (NO) steel sheet of 0.35 mm thick were selected in this study.

3.1. Microstructure and crystallographic texture characterization

The distinctive coarse grain structure and pronounced single texture of GO steel confer properties akin to those of a single crystal, particularly regarding the influence of crystallographic texture on magnetic anisotropy. As a result, Eq. (2) can be directly applied to estimate the permeability at a first approximation. This approach circumvents the necessity for extensive EBSD data collection, which, due to the steel's extremely coarse grains, would require a large sampling area for representativeness. In this framework, the RD aligns with the $\langle 100 \rangle$ directions while the TD corresponds to the $\langle 110 \rangle$ directions. Furthermore, a 55° orientation from the RD, within the rolling plane, approximately aligns with the $\langle 111 \rangle$ directions. Consequently, the permeability measurements of GO steel along the RD, TD, and 55° from RD, at varying magnitudes of magnetic flux density (B), are appropriated as the μ_{100}, μ_{110} and μ_{111} values, respectively, in our FEMTEX model.

A NO steel sample, measuring $10\,\text{mm} \times 11\,\text{mm}$, was prepared for metallographic examination and EBSD analysis of its sheet plane. EBSD data were acquired with a step size of $0.3\,\mu\text{m}$. As depicted in Fig. 2, the inverse pole figure (IPF) maps reveal the microstructure and crystallographic texture of the sample. This data was then transformed into a microstructure in polygonal representation using our EBSD Polygonizer software [17] for input into the FEMTEX model. The resultant microstructural representation, shown in Fig. 2(e), demonstrates a high level of accuracy in the conversion process. Additionally, the mean orientation of each grain, averaged using the Aztec Crystal software from the EBSD data, was utilized to calculate the permeability of individual grains in the FEMTEX model.

3.2. Macroscopic magnetic measurements

The sample dimensions for magnetic property characterization are $50\,\text{mm}\times 50\,\text{mm}$. A vector B–H sensing setup comprising B needle probes and H coils was utilized. This assembly was positioned over the center of the square sample to accurately measure the magnetic flux density and field intensity vectors, **B** and **H**, respectively. A sophisticated digital feedback algorithm facilitated the precise control of the measured **B** field. This allowed for configurations to be either uniaxial at any chosen angle relative to the RD or in a circular pattern, as is standard in such measurements and illustrated in Fig. 3. The measurements in this paper were carried out at 10 Hz. Comprehensive details about these measurement techniques are discussed elsewhere [13].

4. Results and discussion

4.1. Model parameters: single crystal permeability

Fig. 4(a) displays the permeability curves measured from a GO sample along the RD, TD, and at 55° from the RD. These measurements serve as approximations for the single crystal permeability values along the $\langle 100 \rangle$, $\langle 110 \rangle$, and $\langle 111 \rangle$ directions in the FEMTEX model, considering that the orientation of GO grains typically deviates by less than 5–10° from the Goss orientation ($\{110\}\langle 001 \rangle$) [18]. Notably, at magnetic flux densities below $1\,\text{T}$, the permeability μ_{111} exceeds μ_{110}, indicating that the TD, rather than the direction 55° from RD (close to $\langle 111 \rangle$), is the hardest magnetization direction. This phenomenon can be attributed to the bi-axial tensile stress, most pronounced along the RD [19,20], from the coating overshadowing the magnetocrystalline anisotropy and substantially diminishing permeability along the TD. However, at higher magnetic fields, the influence of grain orientation becomes more pronounced, overweighting the stress effects. Fig. 4(b) shows the predicted effective permeability as a function of θ_B, as determined by the FEMTEX model using the measured μ_{100}, μ_{110} and μ_{111} values.

Directly employing experimental data along three specific directions is not feasible for modeling polycrystalline NO steel. Instead, these parameters have been derived through optimization, specifically via nonlinear least-squares fitting of the modeled permeability across angles from 0° to 90° at a 10° interval against experimental measurements. Fig. 5(a) displays the fitted parameters as a function of magnetic flux density. Similar to the GO sample, μ_{100} is significantly higher than both μ_{111} and μ_{110}. Fig. 5(b) compares the fitted permeability with the measured values at only selected B magnitudes for enhanced visibility. While a reasonable fit has been achieved overall, the quality of the fit at lower B values is somewhat less accurate. This discrepancy is likely due to the pronounced stress effects favoring permeability along the RD. However, at higher B values (above $1.3\,\text{T}$), the predicted curves align well with the experimental data.

4.2. Prediction of magnetic flux density distribution in rotational testing samples

Fig. 6 contrasts the magnetic flux density distributions predicted by four distinct material models, with the **B** and **H** vectors represented by small arrows superimposed on the distributions. The isotropic model prediction (Fig. 6(b)) exhibit a uniform B distribution across the sample. In contrast, both the FEMTEX (Fig. 6(a)) and the general-vector (Fig. 6(d)) models predict a pronounced anisotropy, evident in heightened B values averaging around $1.3\,\text{T}$, particularly in diagonal regions. The two-axis model (Fig. 6(c)), on the other hand, foresees a weaker anisotropy in the central area, with a higher average B value, approximately $1.4\,\text{T}$. Notably, both the two-axis and the general vector models are capable of predicting the angles between the **B** and **H** vectors, owing to their effective implementation of tensorial permeability. In comparison, the isotropic and the FEMTEX models predict co-linear **B** and **H** vectors.

4.3. Rotational **BH**

Fig. 7 presents the predicted **H** loci of GO steel in response to a rotational **B** field at $0.3\,\text{T}$ and $1.4\,\text{T}$ using various material models, compared against measurements from a 2D rotational tester. At $0.3\,\text{T}$, GO steel displays pronounced elliptical anisotropy, with the RD and TD

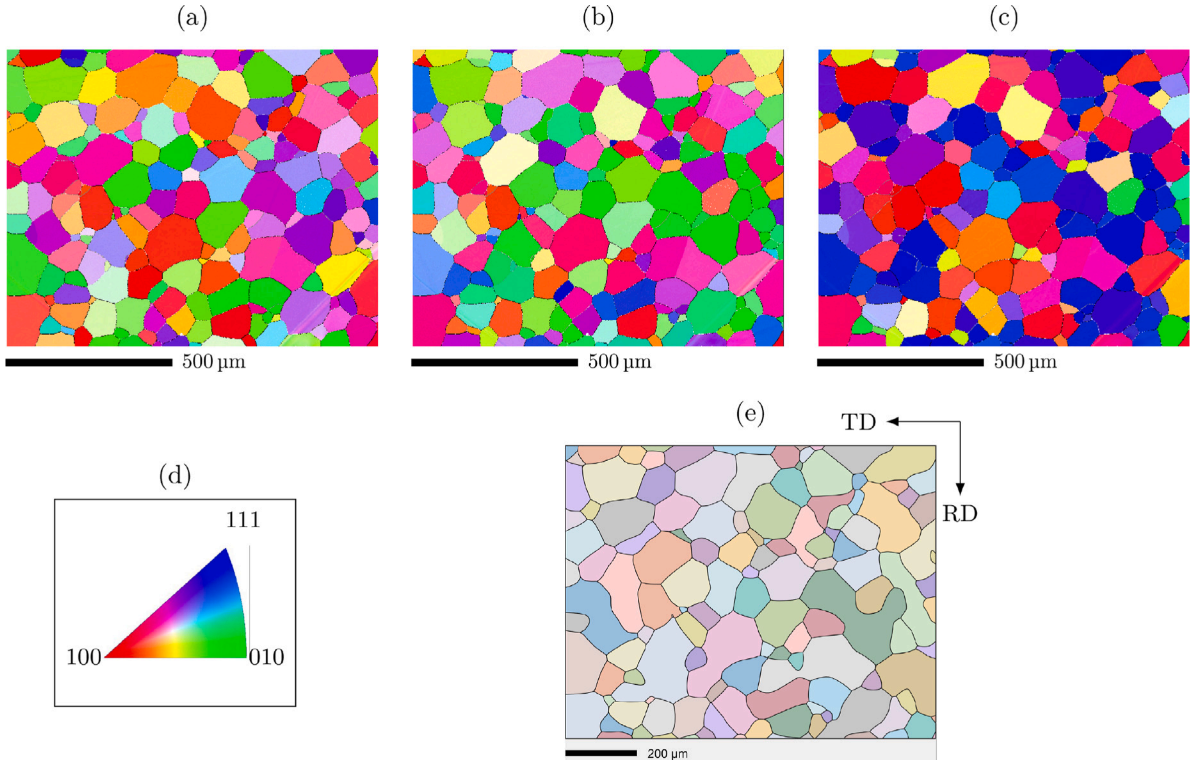

Fig. 2. Inverse Pole Figure (IPF) maps and converted microstructure for integration into the FEMTEX Model. Panels (a) through (c) display the IPF maps for the RD, TD, and ND poles of the NO steel sample, showcasing the crystallographic orientation distribution. Panel (d) provides the color key essential for interpreting these IPF maps. Panel (e) illustrates the microstructure, transformed from the EBSD data and readied for incorporation into the FEMTEX simulation environment. The microstructure visualized in the IPF maps are cohesively represented in the microstructure displayed in Panel (e), underscoring the fidelity of the microstructure conversion. The microstructure is specifically aligned for the RD–TD plane.

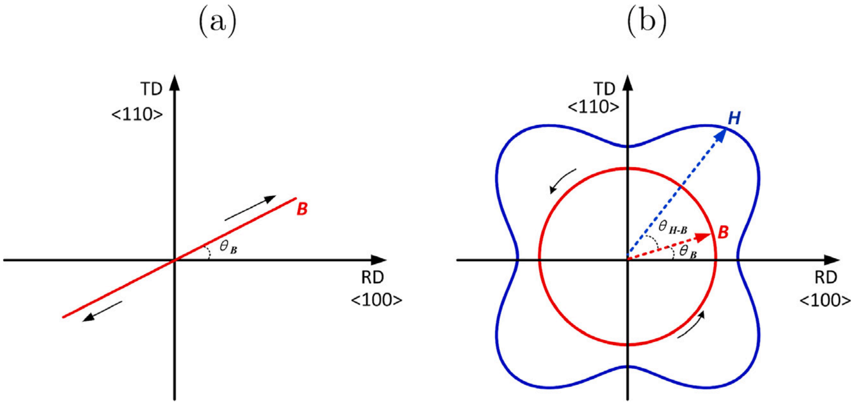

Fig. 3. Schematic representation of magnetic measurements. Panel (a) illustrates uniaxial magnetization, characterized by a magnetic flux density of B_m oriented at an angle θ_B degrees with respect to the RD. Panel (b) shows circular magnetization with a consistent magnetic flux density of B_m. Note that the crystal orientations depicted for the axes are specific to the GO steel sample and do not apply to NO materials.

corresponding to the short and long axes of the **H** magnitude ellipse, respectively. The predictions from both the two-axis and general-vector models align closely with these measurements, whilst the FEMTEX model does not accurately capture this observed anisotropy. At higher magnetic flux density (B), 1.4 T, the material demonstrates increased anisotropy, with a peak in H at 55° from RD, the lowest trough along RD, and a medium trough along TD. This pattern correlates with the hard ($\langle 111\rangle$), easy ($\langle 100\rangle$), and medium ($\langle 110\rangle$) axes in cubic crystals, respectively. Such alignment suggests that crystallographic texture predominantly influences the magnetic anisotropy at high flux densities. At lower B levels, however, the hard direction is less evident in the **H** loci due to the stress effect associated with the coating. The two-axis model, based on the RD and TD measurements, captures this bi-axial anisotropy at lower B. Nevertheless, at higher B, where magnetocrystalline anisotropy surpasses stress-induced effects, the two-axis assumption is inadequate for GO steels since the hard direction in GO lies at approximately 55° relative to RD. Thus, such magnetic anisotropy cannot be accurately described by a diagonal permeability tensor, leading to the limited efficacy of the two-axis model at high B, as evident in Fig. 7(e).

While the FEMTEX model accurately captures the general trend of values along the three directions (RD, TD, and 55° from RD), notable discrepancies are observed in the **H** values between these directions, as shown in Fig. 7(e). These discrepancies could be attributed to the inherent limitations of the FEMTEX model as a scalar permeability model, which invariably predicts **B** to be parallel to **H**. Figs. 7(c) and

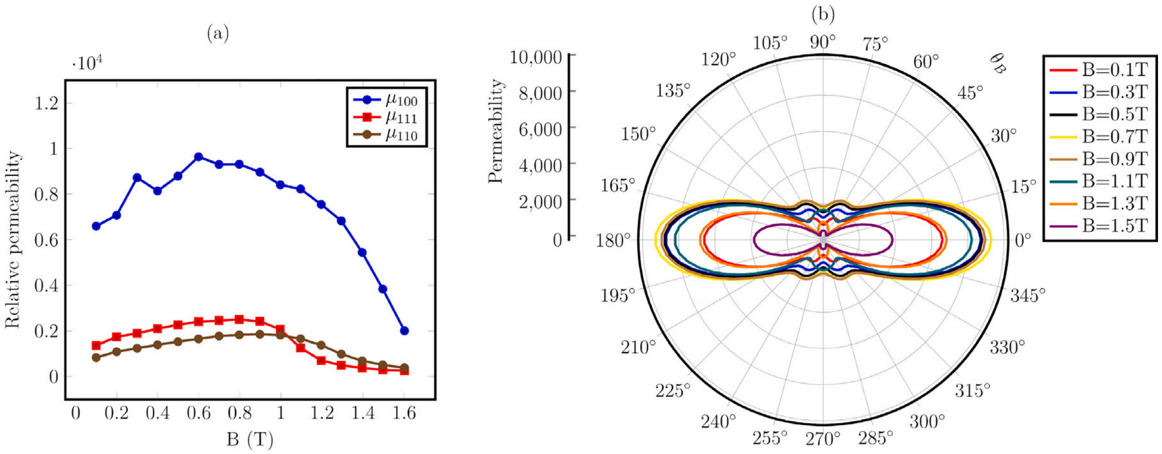

Fig. 4. (a) Illustrates the FEMTEX model parameters for GO steel, showcasing the single crystal permeability along the ⟨100⟩, ⟨110⟩, and ⟨111⟩ directions at various magnetic flux densities (B). (b) Presents the predicted full effective permeability curves as a function of the angle (θ_B) with respect to the RD for different B_m values, demonstrating how permeability varies with both flux density and angular orientation.

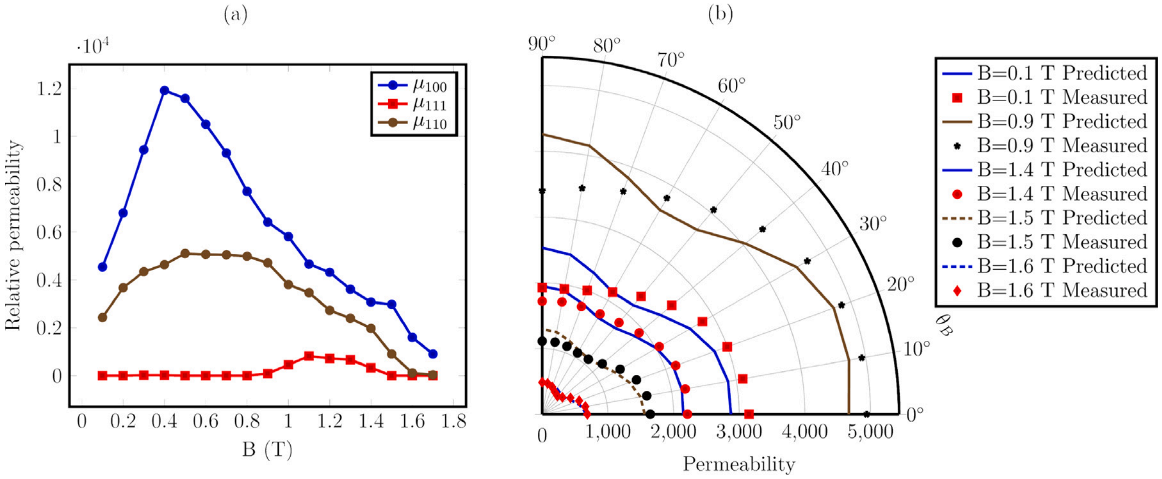

Fig. 5. (a) FEMTEX model parameters for NO steel, demonstrating the fitted single crystal permeability values along the ⟨100⟩, ⟨110⟩, and ⟨111⟩ directions across varying magnetic flux densities (B). (b) Shows the modeled permeability curves as functions of angle (θ_B) relative to the RD, from 0° to 90°, for different magnetic flux densities (B_m). This illustrates the model's fitting accuracy under varying magnetic conditions.

(f) reveal that, except in certain principal directions near RD, TD, and 55° from RD, the angle between **B** and **H**, denoted as θ_{BH}, can rise up to 65° in GO steels. Such significant deviations are not trivial and highlight the inadequacy of scalar permeability models, including both the isotropic and FEMTEX models discussed in this study, in capturing the influence of θ_{BH} on the **H** loci, leading to noticeable inaccuracies in their predictions. Accurate prediction of magnetic anisotropy in GO steels necessitates the use of tensorial permeability. The general-vector model, grounded in extensive experimental data, demonstrates the capability to effectively model materials ranging from weakly anisotropic to strongly anisotropic in nature.

Fig. 8 illustrates the predicted **H** loci of NO steel under a rotational **B** field at both 0.3 T and 1.4 T, using various material models and compared these predictions with actual measurements. Notably, the measured angle θ_{BH} for NO steel is significantly lower than that of GO steel at both flux densities, as depicted in Fig. 8(c) and (f). In this context, the FEMTEX model proves effective in predicting the **H** loci for both 0.3 T and 1.4 T, given that the small θ_{BH} introduces minimal inaccuracies. The general-vector model's predictions also align well with the measurements. However, the two-axis model performs poorly in predicting the **H** loci for NGO steel, tending to overestimate the angle θ_{BH}.

The implementation of the general-vector model necessitates a substantial dataset of 2D vector BH measurements to construct a comprehensive lookup table for precise interpolation. In contrast, a tensorial permeability microstructural model, as proposed in [21], could obviate the need for extensive measurements by predicting permeability tensors based on crystallographic textures and microstructures. Similar to the FEMTEX model, this approach would require only a limited set of material parameters, which are independent of textures and can be readily measured. Currently, work is underway to integrate this predicted tensorial permeability from the microstructural tensorial permeability model into FE device simulations.

5. Case study: Application in the modeling of a permanent magnet motor

To evaluate the effectiveness of our multi-scale approach in capturing magnetic anisotropy amidst complex magnetic fields and geometrical configurations, we have integrated the FEMTEX material model into the FE model of a permanent magnet motor. This implementation primarily aims for qualitative demonstration rather than exhaustive modeling with experimental validation. For this purpose, the model was developed by modifying an example model from the COMSOL Application Library (Application ID: 97091). Fig. 9 depicts the model's

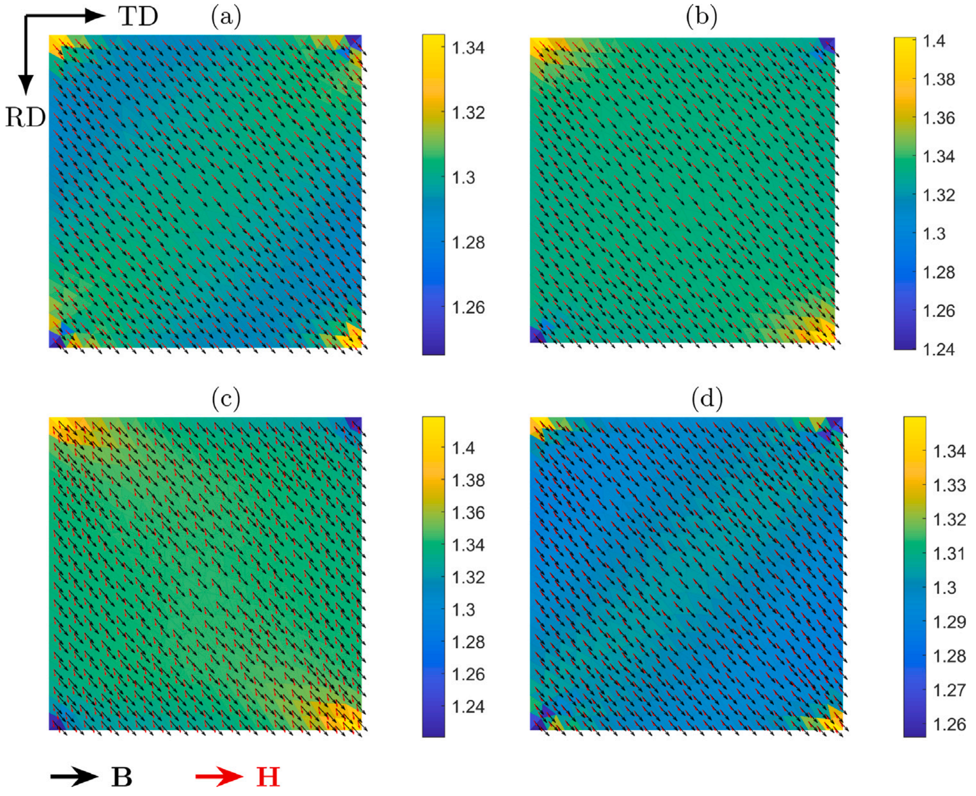

Fig. 6. Comparison of predicted magnetic flux density distributions and vector orientations using four material models. Each panel illustrates the magnitude of **B** (color gradient) and the orientation of the **B** and **H** vectors (represented as arrows) for (a) the FEMTEX model, (b) the isotropic model, (c) the two-axis anisotropic model, and (d) the general vector anisotropic model. This visualization highlights the differences in magnetic behavior predicted by each model.

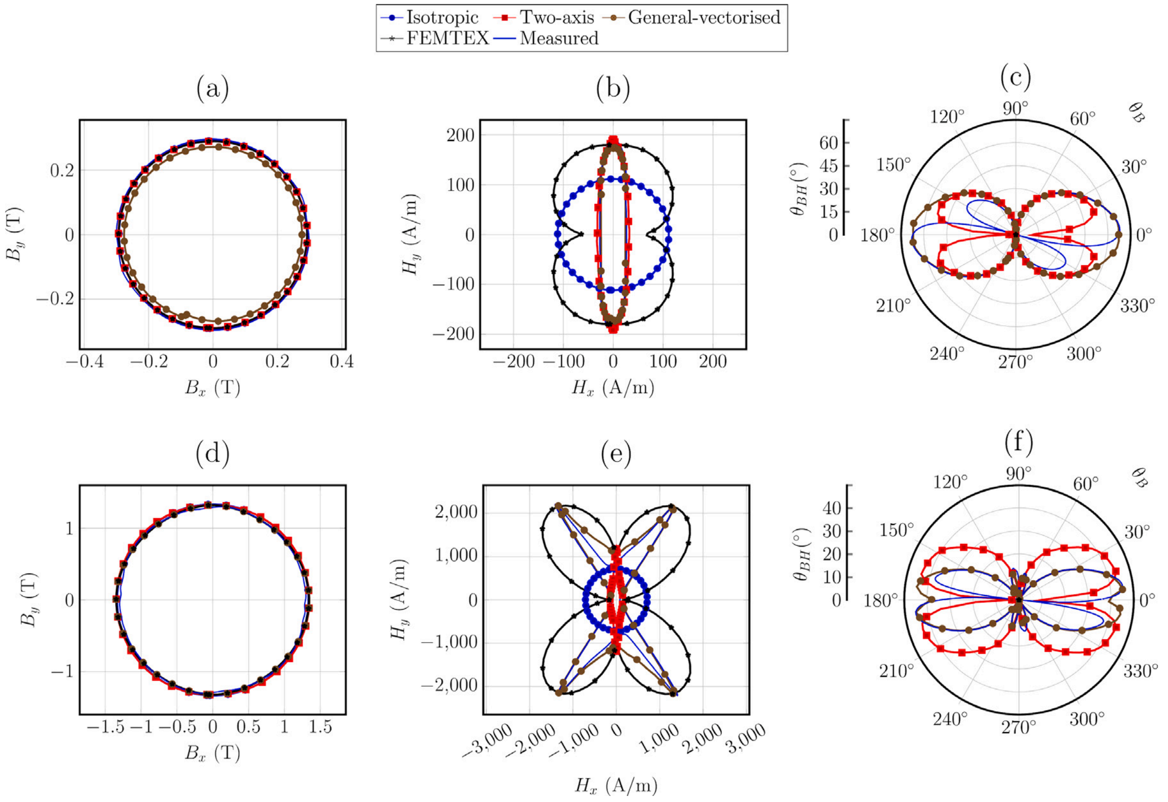

Fig. 7. Comparison of the measured and predicted **B** and **H** loci for GO steel using four different material models, analyzed at both low and high magnetic flux densities. Panels (a) and (d) illustrate the **B** loci at 0.3 T and 1.4 T, respectively. Panels (b) and (e) depict the **H** loci at the corresponding flux densities of 0.3 T and 1.4 T. Panels (c) and (f) show the angle between **B** and **H** vectors, denoted as θ_{BH}, at 0.3 T and 1.4 T, respectively. This set of figures effectively demonstrates the variation in magnetic response at different flux density levels across the material models.

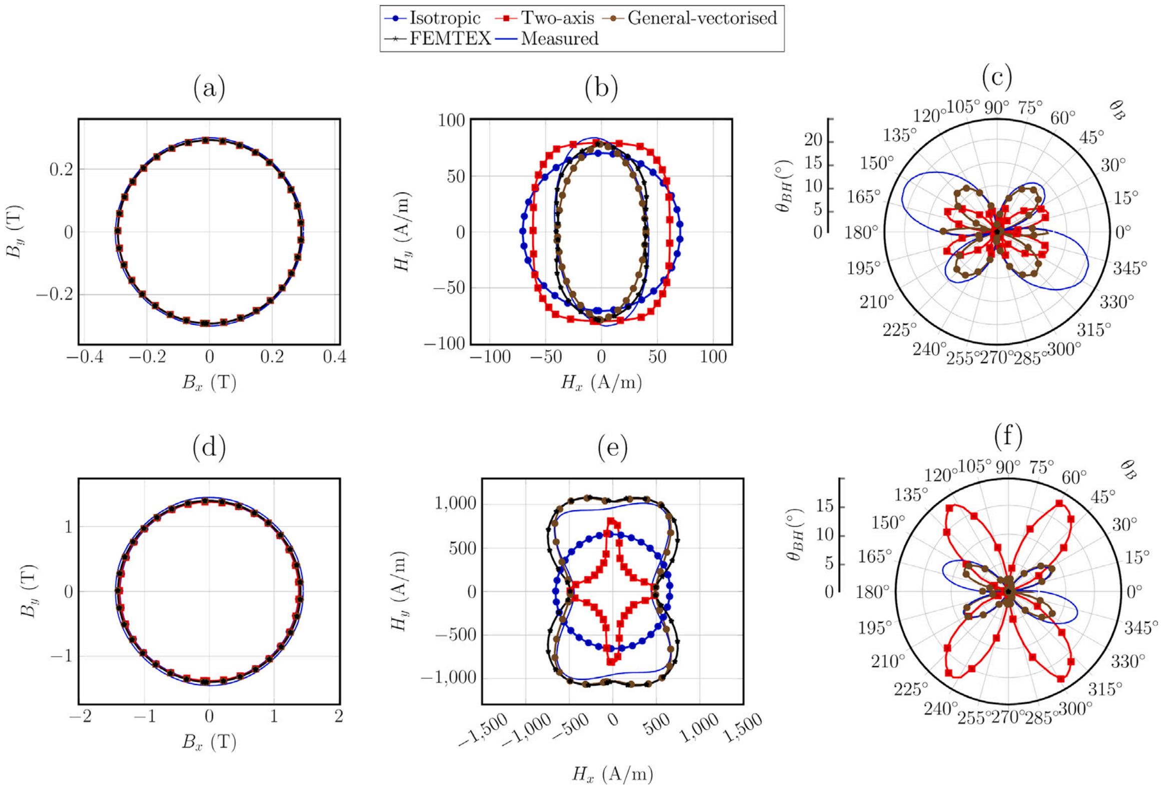

Fig. 8. Comparison of the measured and predicted **B** and **H** loci for NO steel using four different material models, analyzed at both low and high magnetic flux densities. Panels (a) and (d) illustrate the **B** loci at 0.3 T and 1.4 T, respectively. Panels (b) and (e) depict the **H** loci at the corresponding flux densities of 0.3 T and 1.4 T. Panels (c) and (f) show the angle between **B** and **H** vectors, denoted as θ_{BH}, at 0.3 T and 1.4 T, respectively. This set of figures effectively demonstrates the variation in magnetic response at different flux density levels across the material models.

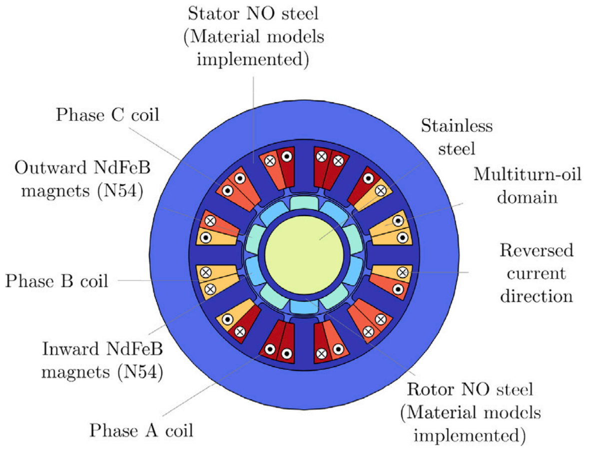

Fig. 9. Geometry and material of a permanent magnet motor model. This illustration details the configuration of various components including stators, rotors, coils, permanent magnets, and shaft.

geometry and materials. The model comprises a stator and a rotor made of NO electrical steels, 24 multi-turn coils for three phases in specific orientations, 5 outward and 5 inward permanent magnets, and a stainless steel shaft. A DC current of 1 A is applied, and a parametric sweep of the initial angle of permanent magnets, θ_{ini}, is conducted. All material parameters, except for those of the stator and rotor, are sourced from the COMSOL Materials Library. For the stator and rotor, two External Materials Libraries incorporating the FEMTEX material model and the isotropic material model for comparison were employed. A detailed description of the example model is available online [22].

Fig. 10 presents the local effective permeability distribution using both the FEMTEX and isotropic material models for the stator and rotor. Notably, a pronounced magnetic anisotropy is evident in the stator laminate when accounting for the crystallographic texture of the electrical steels through the FEMTEX model, with higher permeability predominantly aligning or orienting towards the RD direction (x-axis). Conversely, the isotropic material model, based on measured non-linear scalar BH curve and commonly used in FE modeling of electric motors, fail to represent this magnetic anisotropy.

6. Conclusions

Accurate prediction of magnetic anisotropy and performance in electrical steels, particularly under complex magnetic fields, necessitates the use of anisotropic material models in macroscopic finite element analyses. In this context, we employed the FEMTEX model, a microstructural scalar permeability model, to predict nonlinear scalar anisotropic permeability given the single-crystal permeability values, namely μ_{111}, μ_{110}, and μ_{100}, along the $\langle 100\rangle$, $\langle 110\rangle$ and $\langle 111\rangle$ directions. This model accounts for crystallographic texture and polycrystalline microstructures. FE device simulations using predictions from the FEMTEX model effectively captured the magnetic anisotropy in electrical steels within a rotational tester. This model proved particularly successful when anisotropy was dominated by crystallographic texture and the angle between **B** and **H** was small. However, tensorial permeability becomes essential for accurately predicting anisotropy in scenarios with very strong textures and significant angles between **B** and **H** vectors. The general-vector model, while aligning closely with measurements, requires extensive 2D vector BH measurements for accurate predictions. Conversely, the two-axis model exhibited limitations in predicting the anisotropy of both Grain-Oriented (GO) and Non-Oriented (NO) steels, except in cases with two orthogonal

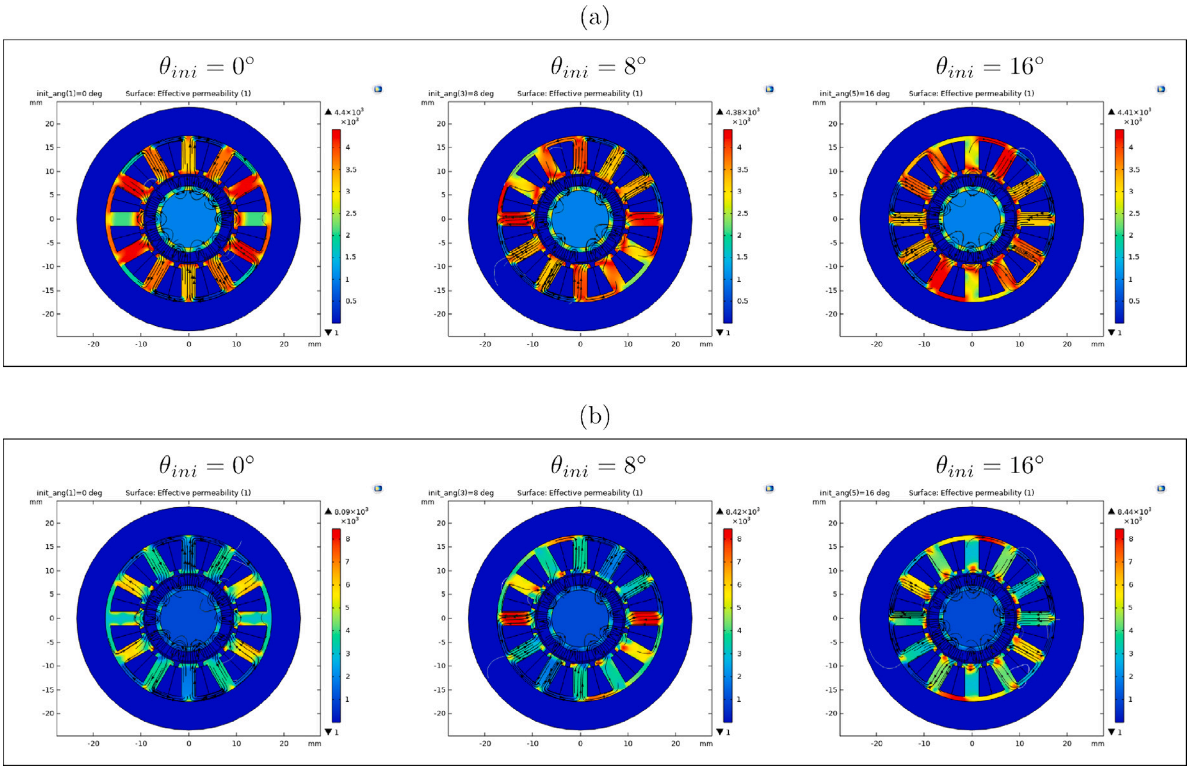

Fig. 10. Comparison of the predicted permeability distribution within the motor using (a) the Isotropic material model and (b) the FEMTEX material model at different initial angles of the permanent magnets. These distributions highlight the impact of the FEMTEX model considering the crystallographic textures on capturing the magnetic anisotropy in the motor components.

principal directions aligning with the easy and hard magnetization directions. The multi-scale approach employing the FEMTEX model also demonstrated proficiency in capturing magnetic anisotropy amidst complex magnetic fields and geometries in a permanent magnet motor. This contrasts with the isotropic model, which is commonly used in FE modeling of electric motors but falls short in accurately representing such anisotropy.

CRediT authorship contribution statement

Shuaichao Yue: Investigation, Software, Validation, Visualization, Writing – original draft, Writing – review & editing. **Jun Liu:** Conceptualization, Software, Visualization, Writing – original draft, Writing – review & editing. **Yongjian Li:** Funding acquisition, Resources, Supervision. **Guodong Liu:** Supervision.

Declaration of competing interest

The authors declare that they have no known competing financial interests or personal relationships that could have appeared to influence the work reported in this paper.

Acknowledgment

The authors extend their gratitude for the support received for this work. This research was partially funded by the National Natural Science Foundation of China under grant number 52130710. Dr. Jun Liu acknowledges the support of the Europe Regional Development Fund through Welsh European Funding Office under the Operation c82117, which sponsored his position from November 2020 to November 2022. Additionally, the authors wish to express their sincere appreciation to Dr. Mohsen A. Jolfaei from the University of Warwick for his invaluable assistance in the collection of Electron Backscatter Diffraction (EBSD) data.

References

[1] Y. Hayakawa, Electrical steels, in: Encyclopedia of Materials: Metals and Alloys, Elsevier, 2022, pp. 208–213, http://dx.doi.org/10.1016/B978-0-12-819726-4.00004-1, URL https://linkinghub.elsevier.com/retrieve/pii/B9780128197264000041.

[2] A. Moses, P. Anderson, K. Jenkins, H. Stanbury, Soft magnetic material, in: Electrical Steels - Volume 1: Fundamentals and Basic Concepts, Institution of Engineering and Technology, 2019, pp. 1–24, http://dx.doi.org/10.1049/PBPO157F_ch1, https://digital-library.theiet.org/content/books/po/pbpo157f. https://digital-library.theiet.org/content/books/10.1049/pbpo157f_ch1.

[3] Y. Guo, J.G. Zhu, J. Zhong, H. Lu, J.X. Jin, Measurement and modeling of rotational core losses of soft magnetic materials used in electrical machines: A review, IEEE Trans. Magn. 44 (2) (2008) 279–291, http://dx.doi.org/10.1109/TMAG.2007.911250.

[4] O. De La Barriere, C. Appino, C. Ragusa, F. Fiorillo, M. Lobue, F. Mazaleyrat, 1-D and 2-D loss-measuring methods: Optimized setup design, advanced testing, and results, IEEE Trans. Magn. 54 (9) (2018) 1–15, http://dx.doi.org/10.1109/TMAG.2018.2846619.

[5] J. Sievert, The measurement of magnetic properties of electrical sheet steel - Survey on methods and situation of standards, J. Magn. Magn. Mater. 215–216 (2000) 647–651, http://dx.doi.org/10.1016/S0304-8853(00)00251-1.

[6] C. Appino, E. Ferrara, F. Fiorillo, C. Ragusa, O. de la Barrière, Static and dynamic energy losses along different directions in GO steel sheets, J. Magn. Magn. Mater. 500 (November 2019) (2020) 166281, http://dx.doi.org/10.1016/j.jmmm.2019.166281.

[7] O. Bíró, S. Außerhofer, K. Preis, Y. Chen, A modified elliptic model of anisotropy in nonlinear magnetic materials, in: P. Dular (Ed.), COMPEL - Int. J. Comput. Math. Electr. Electron. Eng. 29 (6) (2010) 1482–1492, http://dx.doi.org/10.1108/03321641011078553, URL https://www.emeraldinsight.com/doi/10.1108/03321641011078553.

[8] W.A. Pluta, Anisotropy of specific total loss components in Goss textured electrical steel, J. Magn. Magn. Mater. 499 (April 2020) (2020) 166270, http://dx.doi.org/10.1016/j.jmmm.2019.166270.

[9] T. Tamaki, K. Fujisaki, K. Wajima, K. Fujiwara, Comparison of magnetic field analysis methods considering magnetic anisotropy, IEEE Trans. Magn. 46 (2) (2010) 187–190, http://dx.doi.org/10.1109/TMAG.2009.2033558.

[10] K. Fujiwara, T. Adachi, N. Takahashi, A proposal of finite-element analysis considering two-dimensional magnetic properties, IEEE Trans. Magn. 38 (2) (2002) 889–892, http://dx.doi.org/10.1109/20.996229.

[11] S. Higuchi, Y. Takahashi, T. Tokumasu, K. Fujiwara, Comparison between modeling methods of 2-D magnetic properties in magnetic field analysis of synchronous machines, IEEE Trans. Magn. 50 (2) (2014) 373–376, http://dx.doi.org/10.1109/TMAG.2013.2283746.

[12] K. Fujisaki, S. Satoh, M. Enokizono, Influence of vector magnetic property with rotational magnetic flux, magnetic hysteresis and angle difference on stator core loss, J. Jpn. Soc. Appl. Electromagn. Mech. 20 (2) (2012) 360–365.

[13] S. Yue, Y. Li, Q. Yang, K. Zhang, C. Zhang, Comprehensive investigation of magnetic properties for Fe–Si steel under alternating and rotational magnetizations up to kilohertz range, IEEE Trans. Magn. 55 (7) (2019) 1–5, http://dx.doi.org/10.1109/TMAG.2019.2895152, URL https://ieeexplore.ieee.org/document/8641487/.

[14] S. Yue, P.I. Anderson, Y. Li, Q. Yang, A. Moses, A modified inverse vector hysteresis model for nonoriented electrical steels considering anisotropy for FEA, IEEE Trans. Energy Convers. 36 (4) (2021) 3251–3260, http://dx.doi.org/10.1109/TEC.2021.3073349, URL https://ieeexplore.ieee.org/document/9404814/.

[15] J. Liu, J. Shen, C.L. Davis, A finite element microstructure model considering crystallographic texture for forward and inverse magnetic evaluation of anisotropy in steel, SSRN Electronic J. (2019) http://dx.doi.org/10.2139/ssrn.3427484, URL https://www.ssrn.com/abstract=3427484.

[16] L. Daniel, R. Corcolle, A note on the effective magnetic permeability of polycrystals, IEEE Trans. Magn. 43 (7) (2007) 3153–3158, http://dx.doi.org/10.1109/TMAG.2007.896228, URL http://ieeexplore.ieee.org/document/4252285/.

[17] J. Liu, EBSDPolygonizer: Enabling realistic microstructural modelling, SoftwareX 25 (2024) 101622, http://dx.doi.org/10.1016/j.softx.2023.101622, URL https://www.sciencedirect.com/science/article/pii/S2352711023003187.

[18] S. Lee, S.J. Kim, Statistical analysis of misorientation to goss orientation of highly grain-oriented silicon steel, J. Magn. Magn. Mater. 560 (October) (2022) 169563, http://dx.doi.org/10.1016/j.jmmm.2022.169563.

[19] S. Washko, E. Choby, Evidence for the effectiveness of stress coatings in improving the magnetic properties of high permeability 3% Si-Fe, IEEE Trans. Magn. 15 (6) (1979) 1586–1591, http://dx.doi.org/10.1109/TMAG.1979.1060469, URL http://ieeexplore.ieee.org/document/1060469/.

[20] Y. Ding, M. Gallaugher, N. Brodusch, R. Gauvin, R.R. Chromik, Coating induced residual stress in nonoriented electrical steel laminations, J. Mater. Res. 29 (16) (2014) 1737–1746, http://dx.doi.org/10.1557/jmr.2014.218, URL http://link.springer.com/10.1557/jmr.2014.218.

[21] J. Liu, C. Davis, Tensorial permeability microstructure model considering crystallographic texture and grain size for evaluation of magnetic anisotropy in polycrystalline steels, Phil. Mag. 101 (10) (2021) 1224–1244, http://dx.doi.org/10.1080/14786435.2021.1892229, URL https://www.tandfonline.com/doi/full/10.1080/14786435.2021.1892229.

[22] COMSOL, Analyzing electric motor and generator designs (application ID: 97091), 2021, URL https://www.comsol.com/model/analyzing-electric-motor-and-generator-designs-97091.